The Origin of Severe Downslope Windstorm Pulsations

W. R. PELTIER AND J. F. SCINOCCA

Department of Physics, University of Toronto, Toronto, Ontario, Canada

(Manuscript received 4 August 1989, in final form 15 March 1990)

ABSTRACT

Recently reported Doppler lidar observations of the downslope component of flow velocity made during the occurrence of a mountain windstorm at Boulder, Colorado, have established that such storms are characterized by an intense pulsation of windspeed with characteristic period(s) near 10 minutes. Scinocca and Peltier (1989) have independently shown such pulsations to be predicted on the basis of two-dimensional nonhydrostatic numerical simulations in which internal waves launched by stratified flow over smooth topography are forced to exceed critical steepness and, therefore, "break." In the present paper we analyze the physical mechanism that supports this pulsation. As we demonstrate, it is due to Kelvin–Helmholtz instability of the new (quasi-parallel) mean flow that is established in the lee of the obstacle by the wave, mean-flow interaction induced by wave breaking. As such the pulsation represents a secondary instability of the stratified flow in which the primary instability is that associated with the initial transition into the high drag, severe downslope windstorm state. This secondary instability also appears to play a role in determining the maximum intensity that the windstorm may achieve and, therefore, is a crucial ingredient in the wave-turbulence interplay that constitutes the mountain windstorm phenomenon.

1. Introduction

The problem of the origin and nature of severe downslope windstorms such as the chinook of North America, the foehn of Switzerland, and the bora of Yugoslavia has a long history of investigation that has formed a prominent part of the meteorological literature for at least 50 years. One cannot hope to do justice to the very fascinating early work in this area within the confines of this brief introduction to the present paper and so must be content to motivate what follows by focusing attention upon a number of the most recent developments, which it will be our intention to amplify and to extend.

Because of the intensity of the debate concerning the mechanism by which these windstorms are nucleated (Peltier and Clark 1979, 1983; Clark and Peltier 1984; Smith 1985; Durran 1986; Bacmeister and Pierrehumbert 1988, Laprise and Peltier 1989a,b,c), it is perhaps understandable that so little attention has been devoted to the nature of the flow in the severe downslope windstorm state itself. In the present paper, we shall address the issue of the origin of the quasi-periodic time dependence in the strength of the downslope flow that was revealed in the recently published set of very high resolution numerical simulations of fully developed windstorm flows (Scinocca and Peltier 1989). Although some hints of such time dependence had been

previously revealed in the more restricted numerical simulations of Clark and Farley (1984), the explanation of such transience advanced by them was that it was driven by an intrinsically three-dimensional instability of the shear aligned convective-type that had been previously demonstrated to underly the turbulence transition in Kelvin–Helmholtz waves (Peltier et al. 1978, Davis and Peltier 1979, Klaassen and Peltier 1985). The demonstration by Scinocca and Peltier that the windstorm pulsation was also strongly evident in two-dimensional breaking wave simulations very clearly undermines the plausibility of this explanation and it is, therefore, incumbent upon us to provide an alternative. This is the main objective in the present paper. The recent discovery by Neiman et al. (1988) of the same O(10 min) quasi-periodic transience revealed in the simulations of Scinocca and Peltier (1989), in Doppler lidar observations of the wind field during a downslope windstorm at Boulder, Colorado, speaks directly to the relevance of this pulsation to the understanding of detailed observational measurements.

The outline of the paper is as follows: in section 2 we shall begin by briefly reviewing and extending the main results concerning the nature of the windstorm transience that was observed to characterize the flow in the lee of the topography for the three main simulations described in the recently published analyses of Scinocca and Peltier (1989). By spatially and temporally averaging both the horizontal velocity and buoyancy fields in the region between the topographic maximum and the downstream propagating chinook front, we are able to characterize the new mean flow that is

---

Corresponding author address: Professor W. R. Peltier, Dept. of Physics, University of Toronto, Toronto, Ontario M5S 1A7, Canada.

established in the lee of the topographic maximum by the wave, mean-flow interaction induced by wave breaking. Even though the upstream profiles of wind and stability for the three flows analyzed encompass very significant differences, these new mean flows in the lee are shown to exhibit very striking similarities. Of utmost dynamical importance is the fact that the vertical profile of the gradient Richardson number for these new mean states inevitably reveals a sharp minimum either very near to or significantly less than the critical value of 0.25 which, according to the Miles-Howard theorem (Miles 1961; Howard 1961), is the critical value for the onset of Kelvin-Helmholtz instability. The remainder of the paper will involve the detailed demonstration of the, thereafter, obvious fact that the transience in surface wind speed is entirely explicable in terms of this instability. Section 3 presents a brief description of the one-dimensional compressible equivalent of the usual Taylor-Goldstein equation that was used to perform explicit stability analyses on the lee-averaged states obtained in the numerical simulations along with the results of these analyses. Our main conclusions are summarized in section 4.

2. Breaking wave induced mean flows and their superimposed transients

In Scinocca and Peltier (1989) detailed nonlinear numerical simulations of downslope windstorm occurrence were presented for three principal combinations of topographic forcing and upstream profiles of the horizontal component of velocity and the temperature. In each simulation it was demonstrated that an intense quasi-periodic transience in surface wind speed developed to the lee of the topographic maximum and in each case the nature of this transience was strikingly similar qualitatively. Strong pulses of surface wind appeared on the lee slope and propagated downstream with very nearly constant phase speed until they encountered the more slowly propagating chinook front in which they apparently dissipated. Figure 1 presents Hoevmoeller diagrams for surface wind speed from the three simulations discussed in Scinocca and Peltier as a function of range downstream from the topographic maximum. Plates (a), (b), and (c) of this figure are, respectively, for upstream conditions corresponding to the 11 January 1972 windstorm at Boulder, for slightly modified upstream conditions which Scinocca and Peltier (1989) demonstrated to deliver a nearly harmonic downstream propagating pulsation, and for a drastically different mean state characterized by upstream profiles of uniform wind and stability. These different upstream profiles are shown explicitly in Fig. 3 below (solid lines).

On the basis of the Hoevmoeller diagrams in Fig. 1 and from associated time series and their power spectra, we are able to determine the dominant periods, wavelengths and downstream phase speeds of the disturbances that obviously dominate the flow in the slot between the topographic maximum (at $x = 0$ in each case) and the downstream propagating chinook front, behind which the pulsations are inevitably confined. These results are summarized for present purposes in Table 1. In Table 1 (and in what follows) the three flows are denoted by J11 (for the actual 11 January 1972 upstream conditions at Boulder, by MJ11 for the case in which these upstream profiles were slightly modified and for which the pulsation delivered by the numerical integrations was almost perfectly harmonic, and by CNU for the flow with upstream conditions of constant N and U (respectively Brunt-Väisälä frequency and horizontal velocity).

The instantaneous two-dimensional structures of wind (horizontal velocity u) and stability (squared Brunt-Väisälä frequency N^2) are displayed in Fig. 2 at three different times in the course of the MJ11 simulation. Downstream of the topographic maximum, note that the flow has been radically modified from its upstream form. In particular the horizontal velocity has been intensely accelerated in the lowest levels over a height range that extends roughly from the surface to the maximum elevation of the topography. Embedded within this low-level jet are the very high velocity heterogeneities (>80 m s^{-1}) that correspond to the individual pulses seen previously in the Hoevmoeller diagram for this flow (Fig. 1b). Above the low-level jet, and extending to the level of wave breaking, the horizontal velocity has suffered equally extreme deceleration from the values characteristic of the upstream profile. Also embedded within this deep layer of strongly decelerated flow are heterogeneities of horizontal velocity that are strongly correlated with the velocity heterogeneities in the low-level jet. The sense of this correlation is such that regions of anomalously slow (even reversed) flow are found to be located immediately above the high velocity surface pulsations.

Inspection of the N^2 fields for the MJ11 flow (Fig. 2) demonstrates that the low-level jet is coincident with a layer of dramatically enhanced static stability, whereas the thick decelerated layer above has an equally dramatic reduction of stability such that, in fact, $N^2 \leq 0$ in isolated regions. Also, the heterogeneities of N^2 evident in these regions are seen to be highly correlated with the heterogeneities in u. The sense of this correlation is such that regions of static instability overlie regions of reversed flow in the thick decelerated layer. A similar analysis of the J11 and CNU simulations reveals that these observations concerning the nature of the heterogeneities in u and N^2 are equally characteristic of these other flow configurations, a result that clearly suggests a common dynamical origin.

Precisely what physical process these origins might involve is further clarified through analysis of the new mean fields of $\bar{u}$ and $\bar{N}^2$ that are established in the lee of the topography by wave, mean-flow interaction. To this end we have constructed horizontal and temporal averages of the horizontal velocity and potential tem-
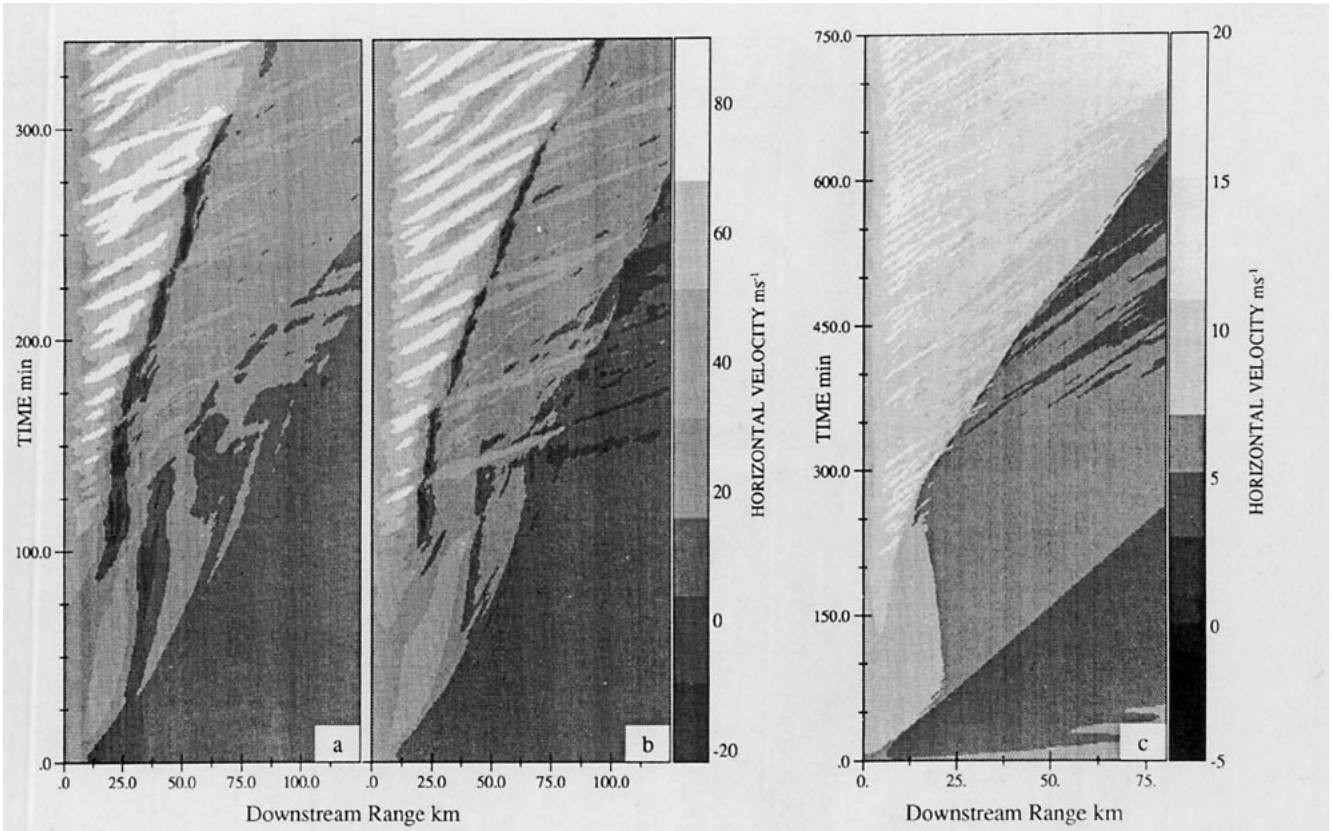
FIG. 1. Hovmoeller diagrams of surface wind speed as a function of range downstream of the topographic maximum for three of the nonlinear simulations presented in Scinocca and Peltier (1989) (a) the 11 January 1972 Boulder windstorm (J11), (b) the modified 11 January 1972 Boulder windstorm (MJ11), and (c) the downslope windstorm initiated with upstream conditions of constant N and U (CNU).

perature fields in the lee of the topographic maximum but upstream of the chinook front for each experiment. These averages are given by

$$\bar{\psi}(z) = \frac{1}{(T_2 - T_1)} \int_{T_1}^{T_2} \left[\frac{1}{(S_2 - S_1)} \right. $$
$$\left. \times \int_{S_1}^{S_2} \psi(x, z, t)dx \right] dt, \quad (1)$$

where $\psi \in \{u, \theta\}$. Table 2 provides detailed information on the extents of the spatial and temporal averaging performed to characterize the new mean flows that are delivered for each of the three cases.

These new mean flows are explicitly presented in Fig. 3, with the J11, MJ11, and CNU cases in plates

TABLE 1.

Run	Period (min)	Phase speed (m s^{-1})	Wavelength (km)
MJ11	12	22.5	16
J11	13–17	18–43	—
CNU	5–20	7	3

a, b, and c, respectively. For each case we have compared the lee-averaged profiles (dashed) with the upstream profiles (solid) of horizontal velocity, temperature, squared Brunt-Väisälä frequency, and gradient Richardson number Ri(z) = $\bar{N}^2(d\bar{u}/dz)^{-2}$. The reader will note by inspection of this Fig. 3 that the nature of the modifications to both horizontal velocity ($\bar{u}$) and stability ($\bar{N}^2$) are qualitatively similar for each of the three cases analyzed. In the lee-averaged horizontal velocity field note the intense deceleration that has occurred between the level of breaking and roughly the maximum topographic elevation, while beneath this latter height the flow has experienced equally dramatic acceleration. The nature of the modifications to the temperature profile from upstream to lee are similarly consistent, with significant warming being characteristic of the downstream profiles. The vertical variation of this general warming beneath the breaking level is such that low-level stability ($\bar{N}^2$) is strongly enhanced whereas midlevel stability in the decelerated zone is significantly reduced. The vertical profile of gradient Richardson number based upon the lee-averaged mean fields establishes very clearly the main point that we will proceed to further elaborate below and which forms the central result of the present paper. Because of the
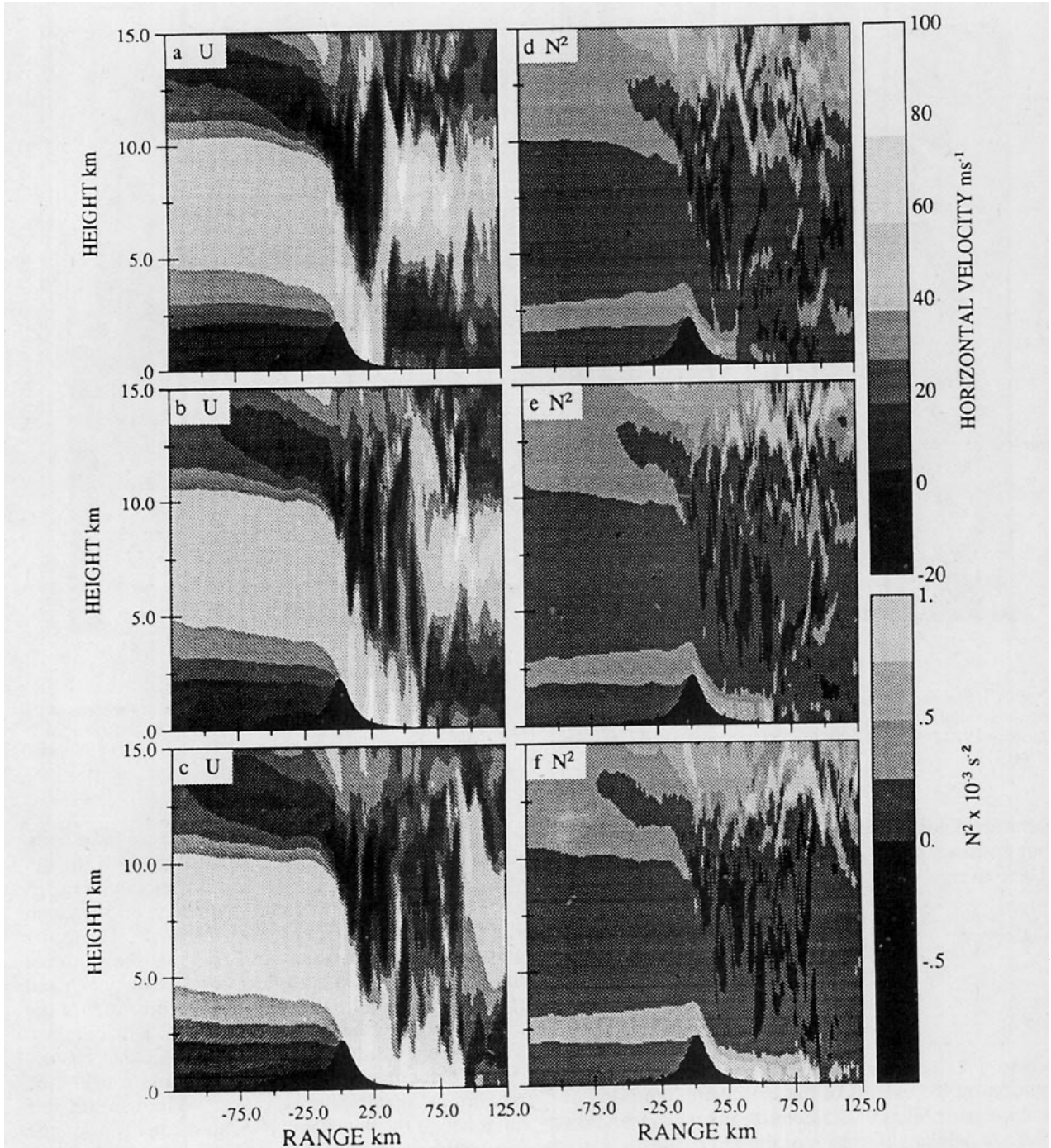
FIG. 2. Total horizontal velocity (a–c) and squared Brunt–Väisälä frequency (N^2) (d–f) fields for the MJ11 case. These are displayed at equivalent model times of (a, d) 198 min, (b, e) 275 min, and (c, f) 342 min.

	Spatial average range $S_1 \rightarrow S_2$ (km)	Temporal average range $T_1 \rightarrow T_2$ (min)	Number of temporal samples N_S
Run			
MJ11	10.0–35.0	198–342	192
J11	10.0–37.5	200–342	19
CNU	3.75–40.0	333–750	24

TABLE 2.

very large vertical shear of the horizontal velocity that develops on the upper surface of the low-level jet, and because of the diminished static stability characteristic of the decelerated zone, the gradient Richardson number profiles characteristic of the lee-averaged states develop a sharp minimum in each of the three cases. For both the J11 and MJ11 cases this minimum is significantly less than the value of 0.25. For the CNU case is very slightly greater than 0.25.
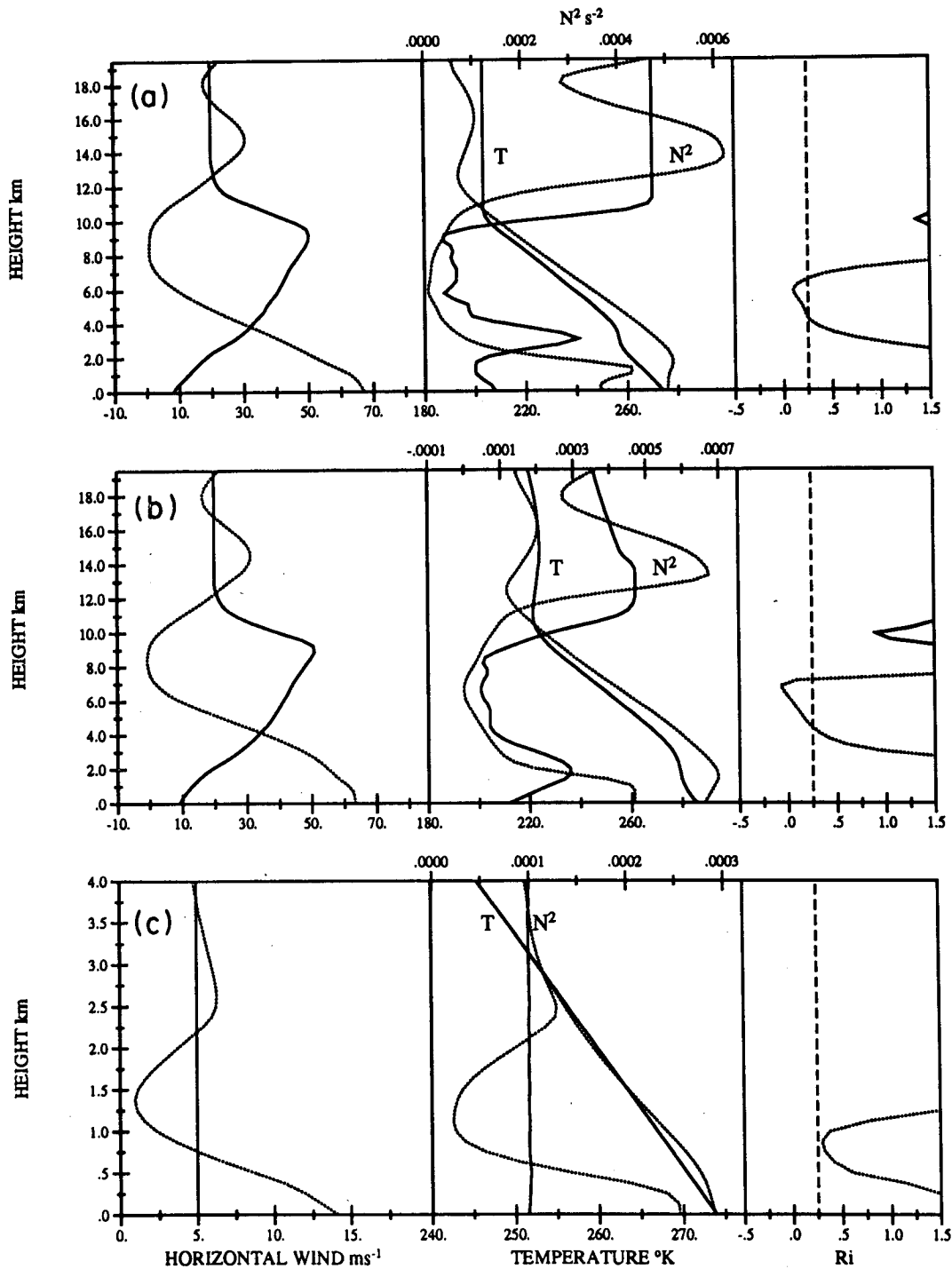
FIG. 3. Upstream profiles (solid lines) and downstream lee-average profiles (dotted lines) of horizontal velocity, temperature, and squared Brunt–Väisälä frequency, and gradient Richardson number. These are displayed for (a) the J11 case, (b) the MJ11 case, and (c) the CNU case.

These characteristics of the flow in the lee of the topography immediately suggest a dynamical explanation of the pulsations that were revealed by the Hoevmoeller diagrams in Fig. 1. The Miles–Howard theorem (Miles 1961; Howard 1961) demonstrates that a stably stratified parallel flow is potentially unstable if $Ri < 0.25$ for some z. Usually this instability is manifest as a Kelvin–Helmholtz wave (e.g., Davis and Peltier 1976, 1977), although significant distortions of this structure may be introduced by the proximity of a (lower) horizontal boundary (Peltier et al. 1978), especially at finite amplitude.

It is clear, however, that the Miles–Howard theorem cannot be directly invoked to account for the presence of the pulses in the nonlinear simulations since the temporally-averaged flow between the topographic maximum and the downstream propagating chinook front is not strictly parallel. In order to establish that the pulses are a manifestation of a Kelvin–Helmholtz instability, we must investigate the local stability of the lee-averaged flows. The most straightforward way to do this is to perform a 1D linear stability analysis of the lee-averaged profiles presented in Fig. 3. Implicit in such analysis is of course the assumption that the flows are parallel. If the wavelength, frequency, phase speed, and growth rate of the fastest growing modes of instability agree with the corresponding characteristics of the pulses determined from the nonlinear simulations, then a causal connection between the pulses and K–H instability can be taken as established. It is this strategy, that is employed in the analyses, that follows. A further discussion of the parallel nature of the flow in the horizontal range over which the lee-average profiles were calculated for the purpose of the stability analysis will be found in section 3d.

Before the stability analyses are conducted, one must first determine, on physical grounds, whether a temporal (real wave number k, complex frequency ω) or spatial (real ω, complex k) analysis is appropriate. From the results of the fully nonlinear simulations one might assume that a spatial stability analysis would be in order since the pulses are seen to grow in intensity as they propagate downstream of the topographic maximum. The circumstances in which a true spatial instability can be physically realized are somewhat subtle, however, and prior to performing the analysis it will be worthwhile to consider them.

The basic formalism required to produce such assessment has come from the analysis of plasma instabilities and is due to Briggs (1964). The basic notion in this theory is that instabilities may be divided into two physical classes: "absolute" and "convective" (Twiss 1951; Landau and Liftshitz 1953; and Sturrock 1958). An absolute instability is defined as one in which growth in time occurs at every point in space due to an initially localized instability. A convective instability is defined as one that grows and propagates away from its origin such that after finite time, at a fixed point in space, the disturbance decays as a function of time (Bers 1973). From such analyses it has been determined (Sturrock 1958) that spatially unstable flow configurations are necessarily of the convectively unstable type. If a flow is absolutely unstable, however, spatial instability can never be realized even though a spatial stability analysis might yield growing modes. It is the temporal stability analysis in such circumstances that would deliver the physical modes of instability. It can be critical, therefore, to assess whether a flow configuration is absolutely or convectively unstable so that a choice between a temporal and spatial analysis can be made on appropriate a priori grounds.

The flow configurations that of concern here, described by the lee-averaged profiles of Fig. 3., are best described as stably stratified shear flows. The absolute versus convective nature of instabilities arising from such stratified parallel shear flows has recently been investigated by Lin and Pierrehumbert (1987). In their analysis, absolute and convective instability regimes were determined as a function of the Richardson number at the point of maximum shear, Ri, and the velocity ratio for the shear layer, C (Lin and Pierrehumbert 1987; Fig. 6). The velocity ratio C is defined by them as $C = (U+ + U-)/|U+ - U-|$, where $U+(-)$ is the asymptotic horizontal velocity above(below) the shear layer. From the results of their analysis it was concluded that for all values of Ri for which the flow was unstable (i.e., $0 \leq$ Ri $\leq \frac{1}{4}$), it was convectively unstable only for $C > 0.76$. From Fig. 3 the value of C may be determined for each of our lee-averaged flows. In all three cases (J11, MJ11, and CNU) it will be seen that $U+$ ~ 0. In such circumstance, $C \sim 1$ and one may conclude that the flow configurations defined by each of the three lee-averaged mean states are convectively and not absolutely unstable. Therefore, the modes derived from a spatial instability analysis will be the ones that are physically realized in such flows.

It is important to note that the analysis of Lin and Pierrehumbert (1987) was performed for an idealized tanhyperbolic shear flow in which the density stratification had the same spatial scale as the shear. The direct application of their results to the more complicated shear flows investigated in this paper is not then strictly valid. For the sake of completeness, therefore, we shall present the results of a temporal stability analysis along with those for the main spatial analysis in the next section. This will also allow us to demonstrate the validity of an asymptotic result originally due to Gaster (1962) that connects spatial and temporal modes when growth rates are small.

3. Windstorm pulsations and parallel shear instability

Although the pulsation phenomenon revealed in our nonlinear time-dependent simulations was a product of anelastic dynamical processes, this being the assumption upon which the numerical model was based, here we have elected to analyze the stability of the mean states in which the pulsation is embedded using a fully compressible linear model. This linear model has been previously exploited in a number of different dynamical contexts (Davis and Peltier 1976; Ley and Peltier 1981; Simard and Peltier 1982). Further modifications were required in the present application. The governing equations of this model are the usual conservation laws for an inviscid, non heat conducting, ideal gas, namely,

$$\rho \frac{d\mathbf{u}}{dt} = -\nabla p + \rho \mathbf{g} \qquad (2a)$$

$$\frac{d\rho}{dt} + \rho \nabla \cdot \mathbf{u} = 0 \qquad (2b)$$

$$\frac{dp}{dt} - \frac{\gamma p}{\rho} \frac{d\rho}{dt} = 0 \tag{2c}$$

$$p = \rho RT, \tag{2d}$$

with d/dt the advective derivative, $\gamma = C_p/C_v$ the ratio of specific heats and the remaining symbols having their conventional meanings. Expanding each of the hydrodynamic fields ρ, p, T, $\mathbf{u}$ as $\psi(x, z, t) = \bar{\psi}(z) + \psi'(x, z, t)$ in two spatial dimensions, with the $\bar{\psi}(z)$ representing the lee-averaged mean state of the downslope storm, we proceed by substituting these expansions into (2) and linearizing this system in the fluctuations $\psi'(x, z, t)$. When the resulting linear equations are Fourier-transformed through application of the following transform pair to each of the fluctuation quantities,

$$\tilde{\psi}(k, z, \omega) = \int_{-\infty}^{+\infty} \int_{-\infty}^{+\infty} e^{-i(\omega t - kx)} \psi'(x, z, t) \, dx dt \tag{3a}$$

$$\psi'(x, z, t)$$
$$= \frac{1}{(2\pi)^2} \int_{-\infty}^{+\infty} \int_{-\infty}^{+\infty} e^{i(\omega t - kx)} \tilde{\psi}(k, z, \omega) \, dk d\omega \tag{3b}$$

and when the resulting system is reduced in the usual way to a single ordinary differential equation for the spectrum of the vertical velocity fluctuation, the governing equation has the form:

$$\frac{d^2\tilde{w}}{dz^2} + A \frac{d\tilde{w}}{dz} + B\tilde{w} = 0. \tag{4}$$

The coefficients in this equation, A and B, are rather complicated functions of the temporal frequency ω and the wavenumber k, either of which may be complex, as is the wavefunction $\tilde{w}$. Explicit expressions for A and B will be found in Eq. (17) of Ley and Peltier (1981) and we shall not reproduce them here.

Equation (4) is the analogue of the Taylor–Goldstein equation of conventional Boussinesq stability theory and may be employed to perform a temporal stability analysis by taking ω complex and determining the circumstances of $\bar{u}(z)$ and $\bar{N}^2(z)$, which allow exponentially growing (in time) eigensolutions to be constructed for the appropriate boundary conditions. It may also be employed to perform a spatial stability analysis by taking k complex and following an identical procedure to construct spatially growing eigensolutions. For the present purpose, as in Davis and Peltier (1976), the presence of the lower boundary (the ground) is important and the appropriate boundary condition on this surface is the kinematic one of $\tilde{w}(k, z = 0, \omega) = 0$. The second boundary condition required to construct solutions to the second-order o.d.e. (4) is a condition of outgoing radiation in the limit $z \to \infty$. As in the previously cited references the eigenproblem posed by (4) with these boundary conditions is solved using a shooting scheme that employs a conventional o.d.e. solver and Müller's method (Müller 1956) to accelerate

convergence to an eigenvalue. For example, in the case of spatial stability we fix k_R (the real part of k) and compute $\tilde{w}(k_I, z = 0, \omega_R)$ by shooting downward from a sufficiently large z so that we may apply the radiation condition analytically. An eigenvalue (k_I, ω_R) for fixed k_R is found when $\tilde{w}_R(k_I, z = 0, \omega_R) = \tilde{w}_I(k_I, z = 0, \omega_R) \equiv 0$.

A useful diagnostic, insofar as physical understanding of the eigensolutions constructed in this way is concerned, follows from a perturbation energy equation that may be derived from the linearized system that follows from (2). This may be written as

$$\frac{\partial E'}{\partial t} + \rho \bar{u}_z u'w' - gw'\theta' \frac{\bar{\rho}}{\bar{\theta}} = -\bar{u}\frac{\partial E'}{\partial x} + \nabla(p'u'), \tag{5}$$

in which

$$E' = \frac{\bar{\rho}}{2}\left[u'^2 + w'^2 + \frac{p'^2}{\bar{\rho}^2 C^2}\right] \tag{6}$$

is the sum of the kinetic and elastic energies for the (generally compressible) perturbation. Defining x-averaging and height integral operators as (for the case of temporal instability)

$$\bar{\psi}(x, z) = \frac{1}{\lambda_x} \int_0^{\lambda_x} \psi(x, z) dx \tag{7a}$$

$$\langle \psi(x, z) \rangle = \int_0^H \phi(x, z) dz, \tag{7b}$$

and operating on (5) with (7), delivers

$$\frac{\partial}{\partial t} \langle \overline{E'} \rangle = -\langle \bar{\rho}\bar{u}_z \overline{u'w'} \rangle + \left\langle g\frac{\bar{\rho}}{\bar{\theta}} \overline{w'\theta'} \right\rangle. \tag{8}$$

Equation (8) demonstrates that the temporal growth of perturbation energy is associated with the extraction of kinetic energy from the mean flow through the action of the Reynolds stress $\overline{u'w'}$ or the extraction of potential energy from the mean flow through the action of the perturbation heat flux $\overline{w'\theta'}$. If the former interaction is dominant the instability is dynamic, whereas if the latter is dominant the instability is static. The utility of (8) is that it can be employed as an a posteriori check on the solutions to the eigenproblem posed by (4). In the case of the temporal instability problem, the perturbation variables have the form:

$$\psi'(x, z, t) = \tilde{\psi}(z)e^{-\omega_I t}e^{i(\omega_R t - k_R x)}. \tag{9}$$

In (8) we then have

$$\frac{\partial\langle \overline{E'} \rangle}{\partial t} = -2\omega_I \langle \overline{E'} \rangle,$$

and we can compute the growth rate of the instability $s = -\omega_I$ as

$$s = \frac{1}{2\langle \overline{E'} \rangle}\left[-\langle \bar{\rho}\bar{u}_z \overline{u'w'} \rangle + \left\langle g\frac{\bar{\rho}}{\bar{\theta}} \overline{w'\theta'} \right\rangle\right]. \tag{10}$$

a. The linear stability of the MJ11 lee profiles

Because the MJ11 case delivers the most intense and regular pulsations, our test of the parallel shear hypothesis will begin by focusing upon this case. The spatial and temporal characteristics of the observed pulsation (as summarized in Table 1) include a horizontal wavenumber $k_R \approx 3.9 \times 10^{-4}$ m^{-1} ($\lambda_x = 2\pi/k_R \approx 16$ km), a temporal frequency $\omega_R \approx 8.4 \times 10^{-3}$ s^{-1} ($T = 2\pi/\omega_R = 12$ minutes), and a horizontal phase speed $C_p \approx 22.5$ m s^{-1}. To begin, consider the spatial stability of the MJ11 lee mean state. Inspection of the time series and their power spectra for surface wind, as a function of downstream location, that were presented in Scinocca and Peltier (1989; Fig. 19) clearly demonstrate that the pulsation grows in amplitude with increasing downstream distance. This analysis can be quantified to obtain a value for the imaginary part of

the horizontal wavenumber k_I. To this end Fig. 4 presents a sequence of five such time series and associated power spectra. The power spectra are based upon the high pass-filtered time series denoted by the dotted lines. Inspection of the power spectra demonstrates that in the range from 12–24 km the 12 minute periodic transient amplifies. Since the amplitude of a spatial instability $A \propto e^{k_I x}$ and since power $P \propto A^2$ we can estimate k_I from $\ln(\sqrt{P/P_0}) = \ln(A/A_0) = k_I x$. In Fig. 5 we have plotted $\ln (A/A_0)$ as a function of downstream position in the range 8.5–36.0 km. A least squares best fit to the data in the range 8.5–16.0 km yields the estimate $k_I \approx 1.97 \times 10^{-4}$ m^{-1}. Inspection of Fig. 5 shows that the exponential growth of the 12 min pulsation persists over only about the first third of the spatial interval for which numerical data are shown. Beyond this range the amplitude appears to saturate. This is consistent with the notion that non-
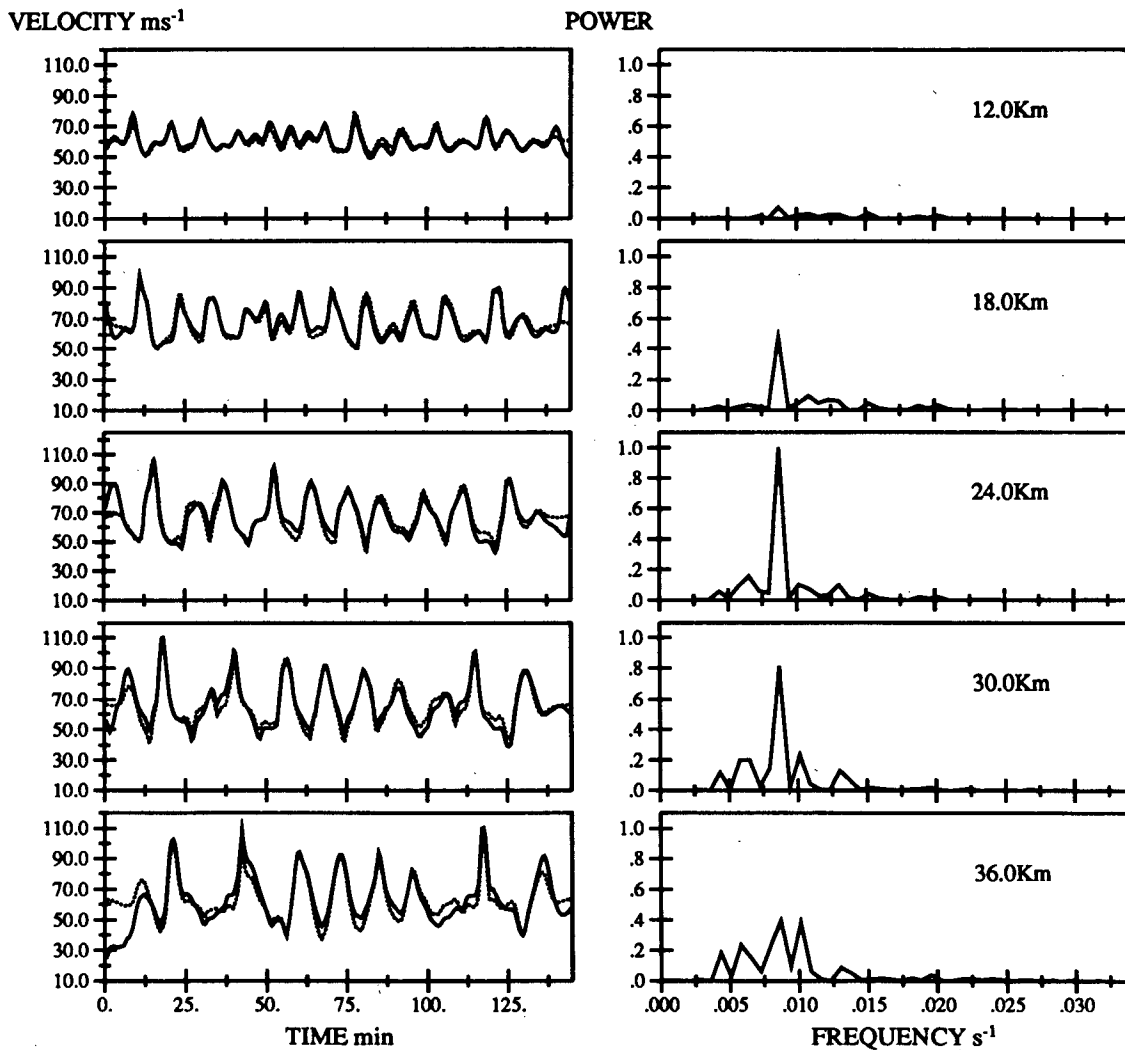
VELOCITY ms⁻¹　　　　　　　　**POWER**

FIG. 4. Time series and associated power spectra of surface wind displayed over the range 12–36 km downstream of the topographic maximum for the last 144 min of model time in the MJ11 nonlinear simulation. Filtered time series (dotted) are displayed as deviations from the mean of the raw time series.

linear effects must eventually arrest the simple exponential growth predicted by linear theory. This view is also consistent with the fact, evident on Fig. 5, that the power spectra markedly broaden as a function of increasing downstream range until by 36.0 km the spectrum is no longer dominated by the strong 12 min component that appears initially on the lee slope of the mountain.

In preparation for the linear stability analysis that will be employed to test the modal structures supported by the MJ11 lee-averaged profiles, we note that critical levels in the background profiles play an important dynamical role in determining such structures. Inspection of the appropriate profiles for the MJ11 case (Fig. 3b) shows that the phase speed of the observed wave, $C_p = 22.5$ m s^{-1}, equals the mean flow speed at two levels, one near 4.5 km and one near 13 km. In order to avoid any complications that might be associated with improper treatment of the uppermost of these critical levels (even though only the lower is within the region in which Ri < 0.25), we have capped the MJ11 profiles with constant $\bar{N}$ and $\bar{u}$ conditions above a height of 15.5 km at which the wind speed is 30 m s^{-1}. These profiles are denoted by the solid lines on Fig. 6. This also helps to obviate an additional complication that arises in the linear model when $k_R \gg k_I$ (or $\omega_R \gg \omega_I$ for temporal instability) and the phase speed equals the wind speed at the level above which constant $\bar{N}$ and $\bar{u}$ conditions are assumed for ease of applying the upper radiation boundary condition.

The main results of the stability analyses of these profiles are shown on Fig. 7. Detailed reconnaisance of the parameter space (k_R, k_I, ω_R) revealed only a single mode of instability. This is represented in Fig.

7a (solid lines) by plots of the variation of the phase speed C_p and the imaginary part of the wavenumber k_I as functions of the real part of the wavenumber k_R. For this mode we note that the most rapid spatial growth obtains with $k_R = 3.79 \times 10^{-4}$ m^{-1} and $\omega_R = 7.86 \times 10^{-3}$ s^{-1} or $C_p = 20.7$ m s^{-1}. This is obviously a very close quantitative agreement with the previously cited parameters from the numerical simulation (3.9 $\times 10^{-4}$ m^{-1}, 8.4×10^{-3} s^{-1}, and 22.5 m s^{-1}, respectively). This comparison is listed in Table 3 for convenience.

Results obtained from a temporal stability analysis of the same lee-averaged profiles for this MJ11 case are superimposed upon those for the spatial stability analysis in Fig. 7 (dotted lines). It will be noted that the results from the temporal stability analysis are almost identical with those of the spatial stability analysis. They are also summarized on Table 3. Although it might appear remarkable that the modes of temporal and spatial instability should be so intimately linked, this is entirely expected in circumstances that were first analyzed by Gaster (1962). Essentially, he demonstrated that, given small growth rates in both the temporal [$\omega_I(T)$] and spatial [$K_I(S)$] analyses, $\omega_I(T)$ and $K_I(S)$ were simply related to the group velocity of the disturbance by

$$\frac{\omega_I(T)}{k_I(S)} = -\frac{\partial \omega_R}{\partial k_R}. \quad (11)$$

We have tested (11) for $k_I(S)$ and $\omega_I(T)$ for the fastest growing mode of instability and at all K_R for which modes of instability of the MJ11 lee profiles exist and found it to be valid to the 1% level. That the spatial and temporal modes of instability in this flow are essentially identical is further confirmed by the eigenfunctions for vertical velocity shown in Fig. 9b (the S and T structures overlap).

Although it is certainly encouraging that the results of the linear stability analysis of the MJ11 lee profiles is in such close agreement with the parameters k_R and ω_R that are characteristic of the pulsation present in this storm, this agreement is less than fully satisfactory because of the implications of the observed rate of spatial growth. The dominant mode is predicted to undergo amplification by a factor of e in $k_R(S)/k_I(S)$ ≈ 248 horizontal wavelengths or $\omega_R(T)/\omega_I(T) \approx 243$ temporal periods. This is approximately two orders of magnitude slower growth than was found to be characteristic of the numerically simulated pulsation (see preceding discussion in connection with Fig. 5).

This final difficulty is in fact rather simply explicable as a consequence of the influence that the instability has on the mean flow that supports it. It is a well documented fact that Kelvin–Helmholtz-like instabilities, feedback negatively upon the mean flow out of which they arise in the sense that the vertical shear of horizontal velocity is sharply diminished by the Kelvin–Helmholtz wave, mean-flow interaction (e.g., Peltier
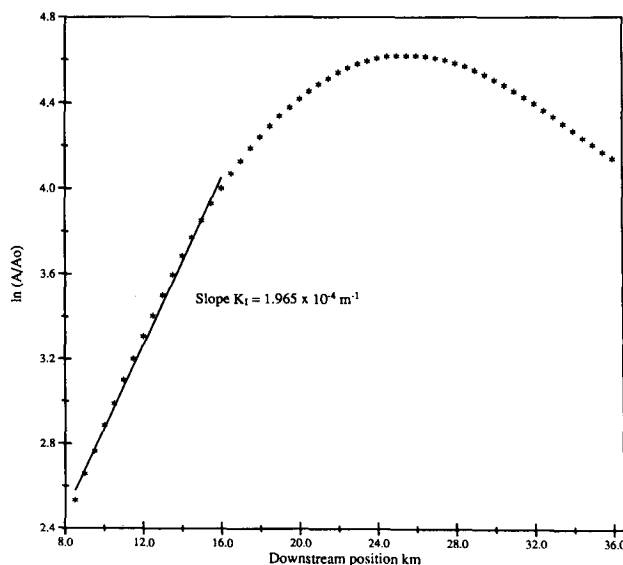

FIG. 5. Plot of $\ln(P/P_0)^{1/2}$ as a function of position downstream of the topographic maximum for the dominant 12 min periodic component of surface wind displayed in Fig. 6.
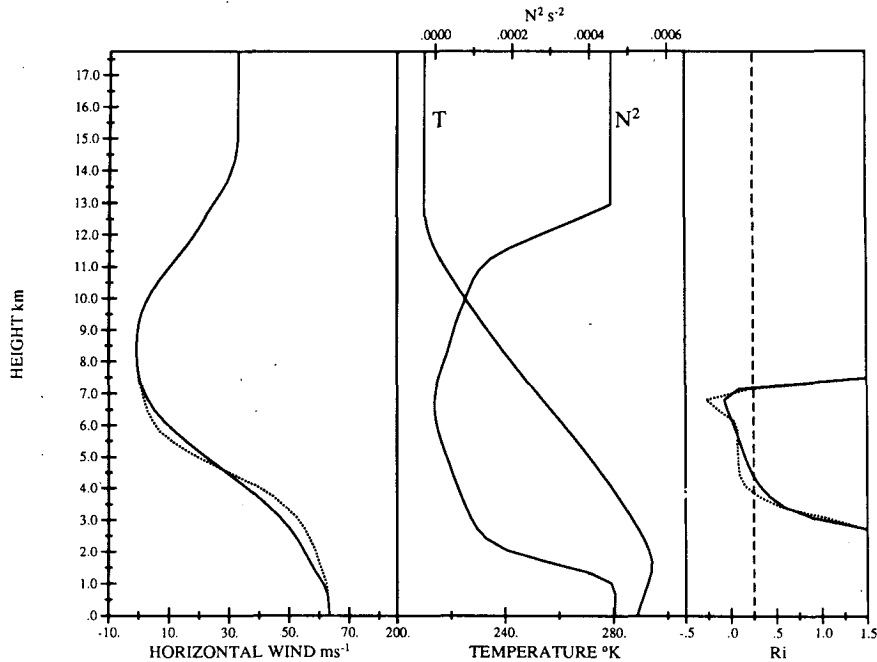
FIG. 6. Lee-averaged profiles capped by constant wind and temperature for the MJ11 case (solid) and the MJ11 case with enhanced velocity shear (dotted) that were employed in the spatial and temporal instability analysis.

et al. 1978; Klaassen and Peltier 1985). To demonstrate that this straightforward explanation of the inadequate growth rate delivered by the initial linear analysis is a viable one, a simple experiment was performed in which the vertical shear of the MJ11 lee-averaged profile was simply enhanced in the vicinity of the maximum in the manner suggested by the above-cited nonlinear life cycle analyses of isolated K–H waves. This modification of the background velocity profile is shown as the dotted line on previously discussed Fig. 6, where it is seen to consist of a smooth deceleration of the flow above the critical level at 4.5 km elevation and a smooth acceleration below. The $\bar{N}^2$ profile is untouched in this experiment and the net effect upon the Richardson number profile is also shown by the dotted curve.

The results of the linear stability analysis of this (shear enhanced) lee-averaged parallel flow are presented on Fig. 8, in which the solid curves show the results for the spatial and the dashed curves for the temporal analyses. Table 3 again provides a summary of results. Both k_R and ω_R and thus $C_p = \omega_R/k_R$ remain in very good agreement with the values of these wave parameters extracted from the simulations. It will be observed on Fig. 8, however, that the spatial and temporal growth rates in the shear enhanced MJ11 flow are nearly two orders of magnitude greater than those delivered by the original profiles. In the shear enhanced case the e-folding distance of the fastest growing mode of spatial instability is now only 3.7 wavelengths, which is within a factor of 2 of the value extracted from the

numerical data shown in Fig. 5. A further minute adjustment of the shear could clearly make this fit exact but this would serve no purpose as the required sensitivity has been established. It will also be noted in connection with Fig. 8 that there are now noticeable differences between the results for the spatial and temporal stability analyses. Figure 8b, for example, which shows normalized eigenfunctions $|\tilde{w}|$ for the fastest growing S (solid line) and T (dotted line) modes, demonstrates significant differences in these two structures. These spatial and temporal inconsistencies are a consequence of the breakdown of the Gaster (1962) result expressed in Eq. (11), a result that is valid only in the weak instability limit. With the enhanced shear the growth rate of the fluctuations is high and the asymptotic result of Gaster no longer obtains.

Figure 9 provides a contoured presentation of the perturbation horizontal velocity field for the fastest growing mode of temporal instability for the MJ11 lee mean state with enhanced wind shear (Fig. 6, dotted lines). Evident by inspection of Fig. 9 is that there are three different elevations at which maximum deviations from the background wind field obtain; the most intense of which is confined to a height range within ±1 km of the critical level at $z = 4.5$ km. The secondary maximum in the horizontal velocity field occurs at the ground ($z = 0$) and, consistent with the structure of the pulsations produced by the numerical simulations (Fig. 3), extend over a depth range of 2 km. Above the critical level a tertiary maximum occurs near a height of 6.5 km.
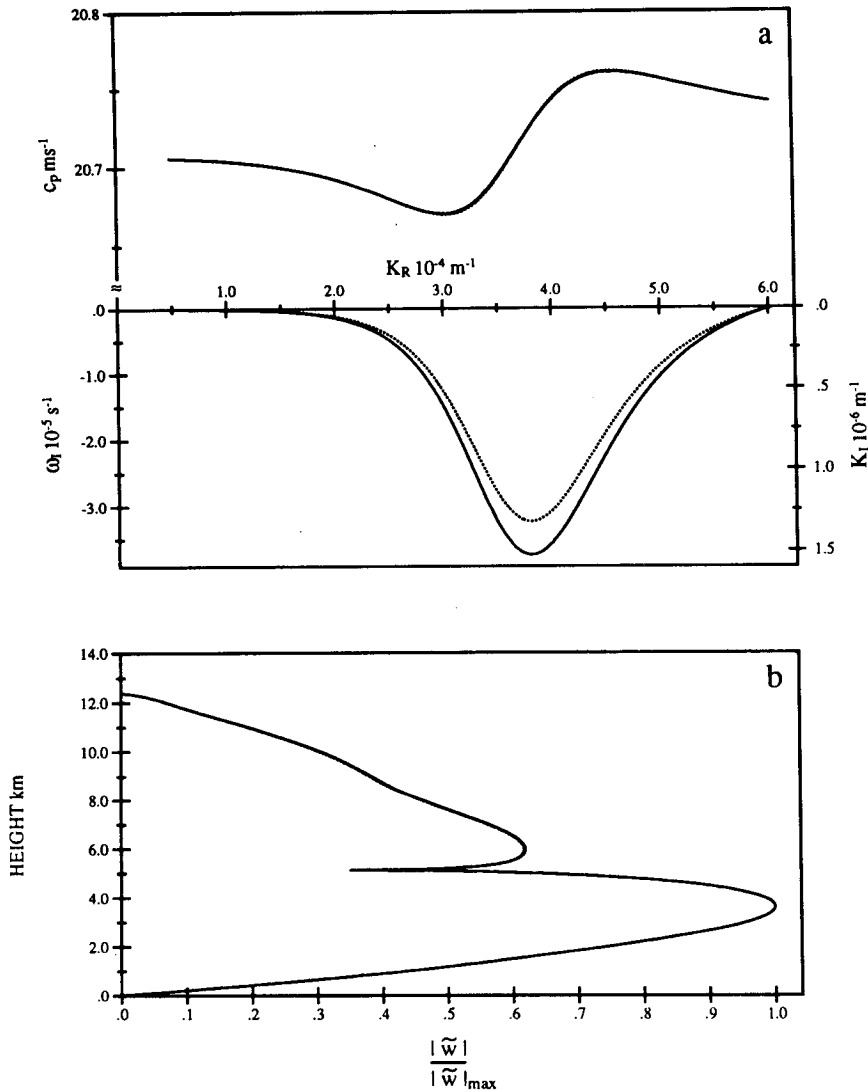
FIG. 7. Results of the spatial (solid lines) and temporal (dotted lines) instability analyses of the MJ11 lee-averaged profiles. Plate (a) displays spatial and temporal phase speeds (c_p) and growth rates (k_I; ω_I) as a function of real wavenumber (k_R). In plate (b) normalized eigenfunction of the fastest growing mode of instability is represented as the magnitude $|w|$ of the vertical velocity perturbation for both the spatial and temporal calculations.

A diagnostic analysis of the energy budget of this mode of parallel shear instability has been performed using the decomposition given in Eq. (10). The results of this analysis, presented in Fig. 9b, demonstrate that for every unit of energy gained by the perturbation, 1.57 units are extracted from the kinetic energy of the

TABLE 3. MJLA Analysis.

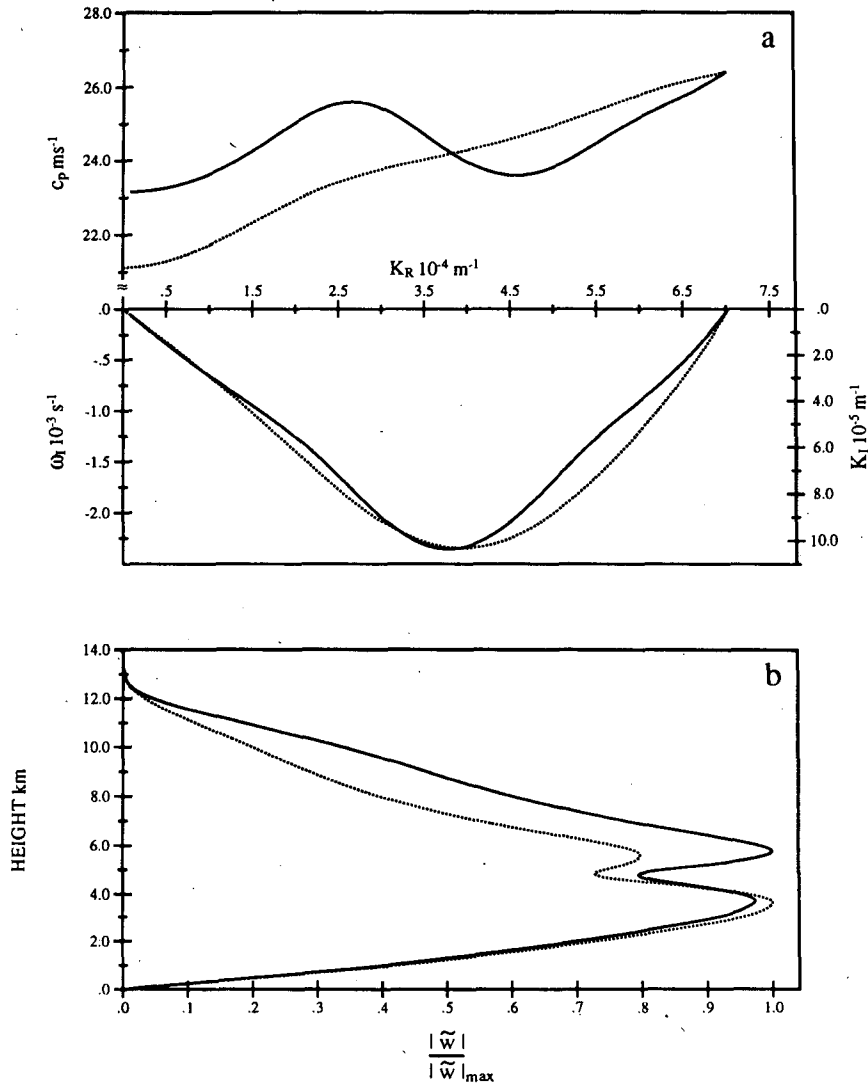| Wave parameters	MJ11 nonlinear simulation	Unmodified MJLA profiles		Modified MJLA profiles	
		Spatial	Temporal	Spatial	Temporal
k_R (m^{-1})	3.9×10^{-4}	3.79×10^{-4}	3.79×10^{-4}	3.78×10^{-4}	3.94×10^{-4}
ω_R (s^{-1})	8.4×10^{-3}	7.86×10^{-3}	7.86×10^{-3}	9.18×10^{-3}	9.56×10^{-3}
k_I (m^{-1})	1.97×10^{-4}	1.53×10^{-6}	—	1.04×10^{-4}	—
ω_I (s^{-1})	—	—	-3.23×10^{-5}	—	-2.35×10^{-3}
C_p (m s^{-1})	22.5	20.7	20.7	24.3	24.3

FIG. 8. As in Fig. 7 except that the MJ11 lee-averaged profiles with enhanced wind shear
(dotted lines Fig. 6) were employed for the spatial and temporal instability analyses.

basic state while 0.57 units are transformed into potential energy. This clearly shows that the mode is a dynamical instability of the parallel-shear-type rather than a static convective instability. The normalized Reynolds stress profile for the perturbation is also displayed in Fig. 10b. According to Eq. (10), a consistency check was performed on the growth rate delivered by the conventional normal mode instability analysis and that delivered diagnostically from the energy density and energy conversion terms. Whereas the eigenanalysis gave $s = -\omega_I = 2.3 \times 10^{-3} \text{ s}^{-1}$ for the fastest growing mode, the diagnostic relation (10) gave $s = 2.1 \times 10^{-3}$ s^{-1} for an error of less than 10%.

Taken together, it is suggested that these results constitute convincing evidence that the harmonic pulsation delivered by the nonlinear time dependent MJ11 windstorm simulations of Scinocca and Peltier (1989)

were caused by excitation of a simple spatial mode of Kelvin–Helmholtz instability of the new mean state induced by the wave, mean-flow interaction caused by wave breaking. However, the MJ11 simulation was rather special in that the pulsation characteristic of it was almost perfectly harmonic. One should, therefore, be interested to know whether similar linear analyses of the J11 and CNU lee-averaged states might provide any explanation for the more variable properties of the pulsations observed in the J11 simulation and for the marked change in horizontal scale of that in the CNU case. These analyses are presented in the following two subsections.

b. *The linear stability of the J11 lee profiles*

The horizontal velocity pulsations obtained in this simulation were characterized (Table 1) by a range of
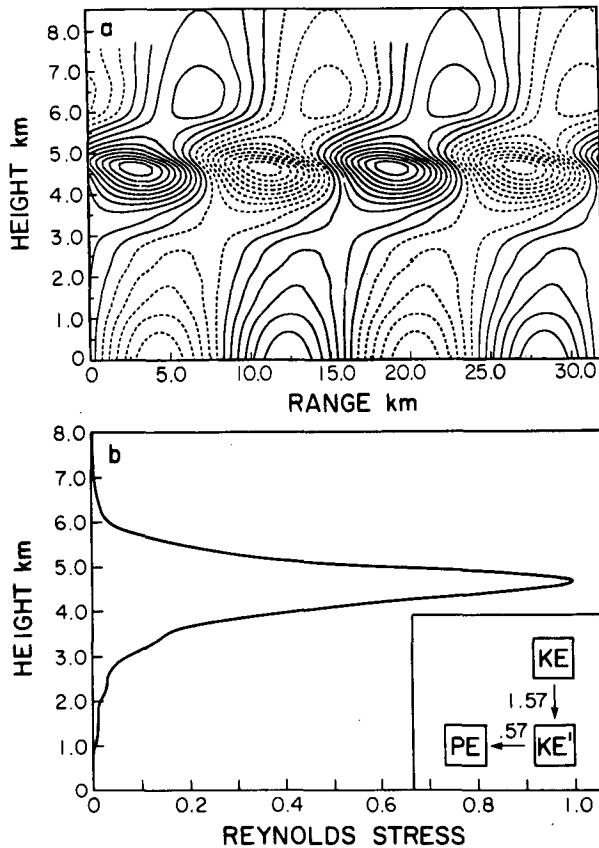
FIG. 9. (a) Perturbation horizontal velocity field for the fastest growing mode of temporal instability for the MJ11 lee mean state with enhanced wind shear and (b) energy conversion diagram and normalized vertical profile of Reynolds stress for the fastest growing temporal mode of instability.

temporal frequencies 6.2×10^{-3} s$^{-1} \leqslant \omega_R \leqslant 8.1 \times 10^{-3}$ s^{-1} and a range of phase speeds 18 m s$^{-1} \leqslant C_{ph} \leqslant 43$ m s^{-1}. The wide range of phase speeds is strikingly evident from the Hoevmoeller diagram for this flow shown as Fig. 1a. Following the procedure described in the last subsection, we subjected the profiles characteristic of the lee mean state for this model storm (Fig. 3a, dashed lines) to a normal mode stability analysis. In this case the direct stability analysis of the numerically derived mean states (solid curves) was shown to deliver no unstable mode for the range of physical parameters that defines this problem. As in the previous example, in which an unstable mode was found to have growth rate at least two orders of magnitude lower than required, we expect the problem to be associated with the fact that the pulsations reduce the vertical shear of horizontal velocity in the mean state from which they derive their energy.

We are therefore led to test the hypothesis by modifying the background profile of horizontal velocity in a manner similar to the modification performed on the lee average MJ11 background described in the previous

section. Table 4 presents the numerical characteristics of the fastest growing modes of spatial and temporal instability determined from the linear stability analysis of these modified profiles along with the corresponding characteristics determined from the nonlinear simulation. It was found that again the spatial and temporal instability analyses predict almost identical wavelength and frequency for the fastest growing mode of instability. For the spatial instability the modal amplitude e-folds every $|k_R(S)/k_I(S)| = 4.4$ horizontal wavelengths while for temporal instability it e-folds every $|\omega_R(T)/\omega_I(T)| = 5$ temporal periods.

As in the previous section a diagnostic energy analysis of the fastest growing mode for this shear enhanced flow was performed. Again the results were characteristic of the same sort of Kelvin–Helmholtz-like instability revealed on the preceding example. The consistency check on the eigenanalysis embodied in Eq. (10) again demonstrated that the results of the energy analysis were (to about 10% accuracy) in accord with the results from the eigenanalysis.

Of course the analysis presented here of the J11 lee-averaged profiles provides no explanation for the wide variability in the phase speed of the individual pulses observed in the corresponding nonlinear simulation; although the theoretically predicted phase speed of the fastest growing mode is well within the observed range. Note, however, that lee-averaged profiles were computed by averaging the fields in the lee of the topography in both space (horizontally) and in time. One must expect that the effective mean flow "seen" by any individual pulse might depart significantly from the long-term temporal average. Viewed from this perspective, the nearly harmonic pulsation that was characteristic of the previously described example must be seen as a rather exceptional case. Indeed, analyses discussed in Scinocca and Peltier (1989) demonstrated how susceptible the regular pulsation of the MJ11 case was to a number of rather minor modifications to the properties of the upstream profiles and topographic forcing.

c. The linear stability of the CNU lee profiles

In concluding the investigation of the parallel shear hypothesis of the origin of severe downslope windstorm

TABLE 4.

Wave parameters	J11 nonlinear simulation	Modified J11 profiles	
		Spatial	Temporal
k_R (m^{-1})	—	3.80×10^{-4}	3.76×10^{-4}
ω_R (s^{-1})	$(6.2-8.1) \times 10^{-3}$	9.55×10^{-3}	9.43×10^{-3}
k_I (m^{-1})	—	8.64×10^{-5}	—
ω_I (s^{-1})	—	—	-1.87×10^{-3}
C_p (m s^{-1})	18–43	25.1	25.1

pulsations, we will briefly focus upon the radically different case presented by the simulation of the phenomenon in a mean flow characterized by upstream profiles of constant Brunt–Väisälä frequency and horizontal velocity. In this case (as summarized in Table 1) all of the pulses of strong surface wind were observed to propagate downstream with the same phase speed C_p $\approx$ 7 m s^{-1}. The most intense pulses were also characterized by a horizontal wavelength $\lambda_x \approx$ 3 km and a period in the range of 5–20 min.

As in the previous example, when these profiles were subjected to a linear stability analysis no modes of instability were found at all. This was expected by virtue of the fact that the gradient Richardson number is nowhere less than 0.25 (solid curve). Therefore, as in the previous examples the hypothesis that shear in the mean state from which the pulsations actually derive their energy had been sharply reduced by their growth was tested.

To this end, the background velocity profile was again modified by enhancing the shear on the interface between the low-level jet and the upper-level decelerated zone to obtain the new horizontal velocity profile. The results obtained from the spatial and temporal stability analyses of these modified profiles are listed in Table 5. The fastest growing spatial and temporal modes again have almost identical properties. In parallel with the previously discussed examples, a summary of modal energetics for the fastest growing (temporal) mode again established that the fastest growing disturbance was a (ground modified) parallel shear instability. Application of Eq. (10) demonstrated consistency in the eigenvalue and energetics analyses at the 6% level.

d. The onset of secondary spatial instability

The linear instability analyses presented in the previous three subsections have provided substantial evidence that the intense pulses of surface wind observed in the three main nonlinear numerical simulations of Scinocca and Peltier (1989) were the result of a surface modified parallel shear mode of spatial instability. In order to demonstrate this result, the instability analyses were restricted to the region of the flow in the lee of the topography where it was most nearly parallel and the pulses of surface wind most regular. Consequently,

the additional interesting point as to the spatial location at which this secondary instability is first initiated has yet to be considered. In this subsection, therefore, the nature of the initial evolution of the spatial instability that is ultimately responsible for the strong pulses of surface wind in the more complex region of the flow directly above the topography is investigated.

In the analysis and discussion of the MJ11 nonlinear simulation presented in Scinocca and Peltier (1989) it was observed that each of the strong pulses of surface wind had originally evolved from a weak disturbance in the flow located slightly upstream of the topographic maximum on the leading edge of the breaking region. In Fig. 10, the horizontal velocity field is presented for the MJ11 case at 3 min intervals for model times of 200–215 min. This sequence is identical to that previously presented in Scinocca and Peltier (1989; Fig. 18) except that here the fields are displayed using an undistorted vertical to horizontal aspect ratio of 1:1. From this perspective, it will be observed that the flow in the downstream range 10–35 km (interval P, Fig. 10) is approximately parallel. This interval corresponds to the region in the flow in which the strong regular pulses of surface wind were observed in the Hoevmoeller diagram (Fig. 1b) and over which spatial averages were calculated (Table 2) for the instability analysis of the MJ11 case described above. In the interval labeled Q–P on Fig. 10, the early evolution of the instability responsible for the strong pulses of surface wind is observed to occur. Modes of instability in this region of the model domain sense a background flow and lower surface that slowly vary in the downstream direction.

Even though the background flow appears more complex in the range over which the spatial instability initially onsets (Q–P), it may be demonstrated that the flow conditions in this region of the model domain are sufficient to support the same type of parallel shear flow instability that was found to be characteristic of the flow in the interval P. In Fig. 11 temporally-averaged vertical profiles of u, θ, N^2 and Ri are displayed in the range extending from 10 km upstream to 10 km downstream of the topographic maximum at intervals of 2.5 km. The temporal averages were performed over a time span equivalent to that previously employed in the instability analysis of the MJ11 case and documented in Table 2. The far upstream profiles imposed on the flow (heavy lines) have been included for reference. It is immediately apparent from Fig. 11 that the temporally-averaged background flow in the high drag regime is a slowly varying function of horizontal position in the interval Q–P. Because of this slow variation, it would seem a reasonable approximation to consider the background flow in this range to be locally parallel.

Under this quasi-parallel approximation, one may consider the dynamical stability of the temporally-averaged background profiles as a function of horizontal

TABLE 5.

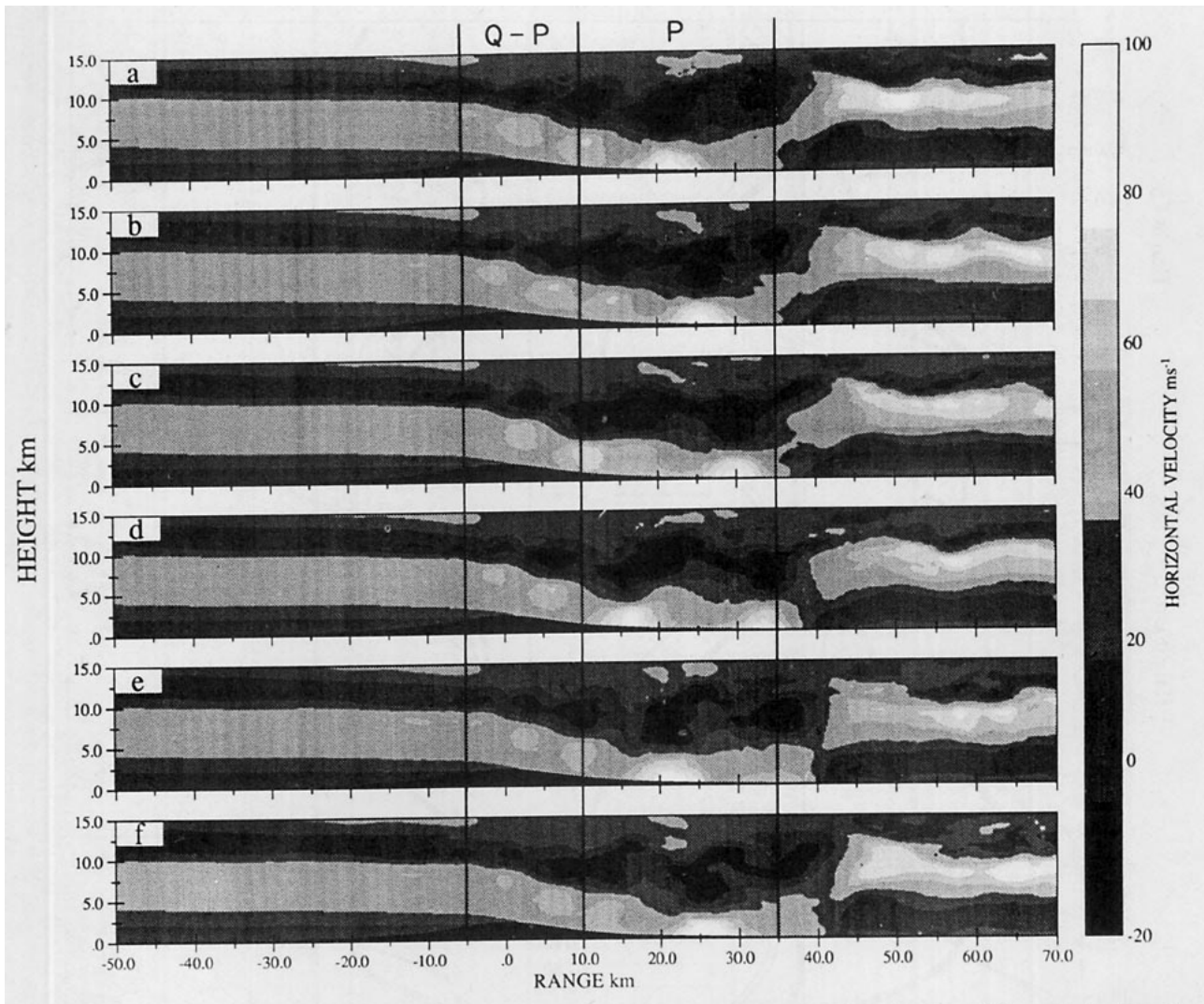| Wave parameters	CNU nonlinear simulation	Modified CLA profiles	
		Spatial	Temporal
k_R (m^{-1})	2.09 × 10^{-3}	2.13 × 10^{-3}	2.20 × 10^{-3}
ω_R (s^{-1})	5.24 × 10^{-3}–2.09 × 10^{-2}	1.61 × 10^{-2}	1.65 × 10^{-2}
k_I (m^{-1})	—	3.10 × 10^{-4}	—
ω_I (s^{-1})	—	—	−1.92 × 10^{-3}
C_p (m s^{-1})	7.0	7.56	7.52

FIG. 10. Total horizontal velocity field from the MJ11 nonlinear simulation. (a)–(f) span 200–215 min of model time at 3 min intervals. The range labeled P on the figure corresponds to the parallel portion of the downstream range over which the spatial averages were calculated to perform the linear instability analysis in section 3a. The interval labeled Q–P on the figure corresponds to the quasi-parallel portion of the flow where the spatial instability responsible for the strong pulses of surface wind initially onsets.

range in the interval Q–P. In Fig. 11 it is revealed that the necessary condition for dynamic instability $Ri \leqslant \frac{1}{4}$ is first satisfied within the interval Q–P between 7.5 and 5.0 km upstream of the topographic maximum at an elevation near 9 km. It is at this location in the flow where the onset of the instability that ultimately produces the strong pulses of surface wind was first observed in Fig. 10. As one looks to positions further displaced in the downstream direction, it will be seen that this criterion is always satisfied by the background flow in the interval Q–P. Fig. 11 also reveals, however, that the elevation and depth through which $Ri \leqslant \frac{1}{4}$ is achieved by the background flow is a function of downstream position. As a result, the parameters that characterize the fastest growing mode of instability will in general vary slowly as a function of downstream position in the range Q–P. This would indicate that no

one mode of spatial instability could dominate the spectrum in this range. This is consistent with the observation from the MJ11 nonlinear simulation that the disturbances responsible for the strong pulses of surface wind seem to grow quite quickly as they pass from the region Q–P (where there is an evolution of the fastest growing mode of spatial instability) into the range P (where the parallel nature of the flow allows the selection of one mode, which thereafter dominates the spectrum).

While this analysis has helped in understanding the evolution of the instability in this more complicated region of the flow, it must be made clear that the spatial instability mechanism cannot account for the initial onset of the disturbances far above the topographic maximum. Such a mechanism can only selectively amplify modes from preexisting disturbances (or white
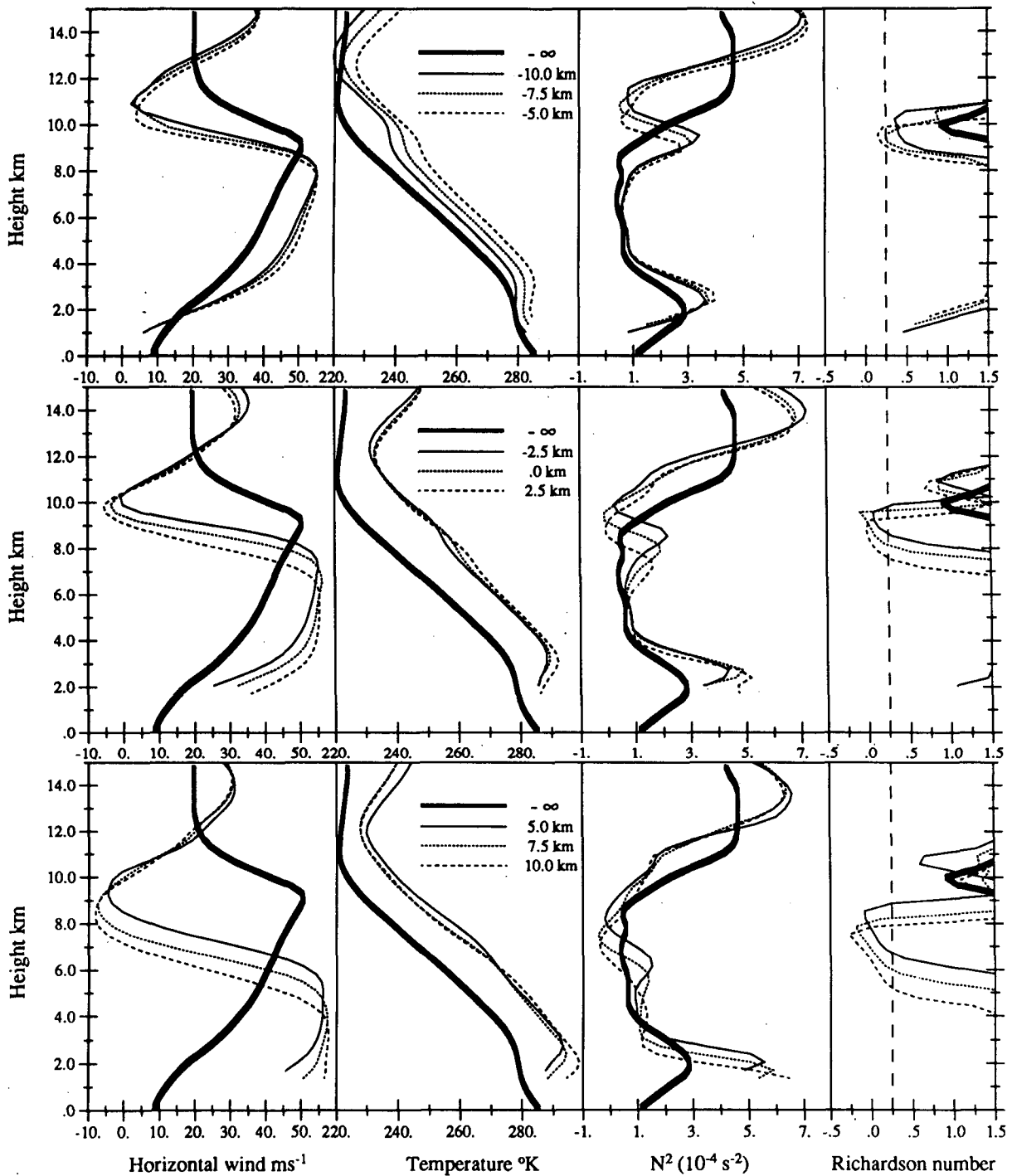
FIG. 11.Temporally-averaged profiles of U, θ, N^2 and Ri for the MJ11 nonlinear simulation at 2.5 km intervals in the range extending from 10 km upstream to 10 km downstream of the topographic maximum (interval Q-P). Heavy lines represent the imposed upstream profiles used to initiate the nonlinear simulation.

noise) already present in the flow. The elevation above the topographic maximum where these initial disturbances are observed however is known to be the most turbulent region of such downslope windstorm flows (e.g., Lilly 1978).

4. Conclusions

The analyses presented in section 3 provide compelling evidence that the intense pulsation in windspeed that was shown to be characteristic of the mature

downslope windstorms delivered by two-dimensional numerical simulations of breaking, topographically forced internal waves. This is caused by Kelvin–Helmholtz instability on the shear interface between the low-level jet and the upper-level decelerated layer, which are induced by the wave, mean-flow interaction associated with wave breaking.

This secondary instability plays a very important role in the evolution of the mature windstorm. For example, in each of the simulations presented in Scinocca and Peltier (1989) it was observed that the chinook front propagated with nearly uniform speed in the downstream direction. The K–H instability is most probably responsible for this phenomenon. As these disturbances propagate downstream they transport x-momentum in the x-direction (via $\rho_0\overline{u'u'}$, where the average is now in time). The divergence of $\overline{\rho u'u'}$ across the chinook front then induces the deposition of horizontal momentum at this location and causes the region of modified flow to extend further downstream.

This paper has focused exclusively upon the connection between the secondary K–H instability and the quasi-periodic fluctuations in surface wind observed during actual events. The action of this instability, however, could have far reaching implications for our understanding of the transition into the severe downslope windstorm configuration itself. The stability analyses presented here also suggest that, in the "high drag regime," it is the Kelvin–Helmholtz instability that regulates the strength of the storm. Since this instability mixes downslope momentum in the vertical direction, thus decelerating the low-level flow and accelerating the fluid in the overlying mixed layer, it provides a negative feedback mechanism by which a balanced "high drag state" can be achieved.

While this conclusion seems physically reasonable, it must be clearly understood that it is based solely on the observed evolution of the K–H mode during the mature state of the windstorm when the drag curve has "saturated." In all of the nonlinear simulations presented in Scinocca and Peltier (1989), it was found that the pulses were observed to form during the earliest phases of the evolution of the windstorm in the elevated breaking region, soon after the primary wave field goes unstable above the topography. The 2D linear stability of the primary wave field has recently been investigated by Laprise and Peltier (1989a,b,c). They showed that the flow becomes unstable to a deep mode of dynamic instability as streamlines overturn. It was this mode of instability that they postulated to be responsible for the evolution of the flow away from the steady state solution predicted by Long (1953) and into the high drag state characteristic of downslope windstorms. Since the K–H instability analyzed here is also a dynamic instability, it would seem possible that it is simply the time-evolved form of the deep mode of instability documented by Laprise and Peltier (1989a). In the future, it is intended to make this the subject of further study

in order to further clarify the nature of the instability that appears to underlie the initial transition into the high drag regime.

REFERENCES

Bacmeister, J. T., and R. T. Pierrehumbert, 1988: On high-drag states of nonlinear stratified flow over an obstacle. *J. Atmos. Sci.*, **45**, 63–80.

Bers, A., 1973: Theory of absolute and convective instabilities. *International Congress on Waves and Instabilities in Plasmas*, Innsbruck, Austria, B1–B52.

Briggs, R. J., 1964: *Electron-Stream Interactions in Plasmas.* MIT Press.

Clark, T. L., and W. R. Peltier, 1977: On the evolution and stability of finite-amplitude mountain waves. *J. Atmos. Sci.*, **34**, 1715–1730.

——, and R. D. Farley, 1984: Severe downslope windstorm calculations in two and three spatial dimensions using anelastic interactive grid nesting: a possible mechanism for gustiness. *J. Atmos. Sci.*, **41**, 329–350.

——, and W. R. Peltier, 1984: Critical level reflection and the resonant growth of nonlinear mountain waves. *J. Atmos. Sci.*, **41**, 3122–3134.

Davis, P. A., and W. R. Peltier, 1976: Resonant parallel shear instability in the stably stratified planetary boundary layer. *J. Atmos. Sci.*, **33**, 1289–1300.

——, and ——, 1977: Effects of dissipation on parallel shear instability near the ground. *J. Atmos. Sci.*, **34**, 1868–1884.

——, and ——, 1979: Some characteristics of the Kelvin-Helmholtz and resonant overreflection modes of shear flow instability and of their interaction through vortex pairing. *J. Atmos. Sci.*, **36**, 2394–2412.

Durran, D. R., 1986: Another look at downslope windstorms. Part I: The development of analogs to supercritical flow in an infinitely deep, continuously stratified fluid. *J. Atmos. Sci.*, **43**, 2527–2543.

Gaster, M., 1962: A note on the relation between temporally-increasing and spatially-increasing disturbances in hydrodynamic stability. *J. Fluid Mech.*, **14**, 222–224.

Howard, L. N., 1961: Note on a paper of John W. Miles. *J. Fluid Mech.*, **10**, 509–512.

Klaassen, G. P., and W. R. Peltier, 1985: The onset of turbulence in finite-amplitude Kelvin–Helmholtz billows. *J. Fluid Mech.*, **155**, 1–35.

Landau, L. D., and I. M. Lifshitz, 1953: Electrodynamics of continuous media. (in Russian) *G.I.T.T.L.*

Laprise, R. J., and W. R. Peltier, 1989a: The linear,stability of nonlinear mountain waves: implications for the understanding of severe downslope windstorms. *J. Atmos. Sci.*, **46**, 545–564.

——, and ——, 1989b: The structure and energetics of transient eddys in a numerical simulation of breaking mountain waves. *J. Atmos. Sci.*, **46**, 565–585.

——, and ——, 1989c: On the structural characteristics of steady finite-amplitude mountain waves over bell shaped topography. *J. Atmos. Sci.*, **46**, 586–595.

Ley, B. E., and W. R. Peltier, 1981: Propagating mesoscale cloud bands. *J. Atmos. Sci.*, **38**, 1206–1219.

Lilly, D. K., 1978: A severe downslope windstorm and aircraft turbulence induced by a mountain wave. *J. Atmos. Sci.,* **35,** 59–77.

——, and J. B. Zipser, 1972: The front range windstorm of 11 January 1972—a meteorological narrative. *Weatherwise,* **25,** 56–63.

Lin, S. J., and R. T. Pierrehumbert, 1987: Absolute and convective instability of inviscid stratified shear flows. *Proc. Third International Symposium on Stratified Flows,* Pasadena.

Long, R. R., 1953: Some aspects of the flow of stratified fluids, a theoretical investigation. *Tellus,* **V,** 42–58.

Miles, J. W., 1961: On the stability of heterogeneous shear flows. *J. Fluid Mech.,* **10,** 496–508.

Muller, D. E., 1956: A method for solving algebraic equations using an automatic computer. *Mathematical Tables and Aids to Computation,* **10,** 208–215.

Neiman, P. J., R. M. Hardesty, M. A. Shapiro and R. E. Cupp, 1988: Doppler lidar observations of a downslope windstorm. *Mon. Wea. Rev.,* **116,** 2265–2275.

Peltier, W. R., and T. L. Clark, 1979: The evolution and stability of finite-amplitude mountain waves. Part II: Surface drag and severe downslope windstorms. *J. Atmos. Sci.,* **36,** 1498–1529.

——, and ——, 1983: Nonlinear mountain waves in two and three spatial dimensions. *Quart. J. Roy. Meteor. Soc.,* **109,** 527–548.

——, J. Halle and T. L. Clark, 1978: The evolution of finite amplitude Kelvin–Helmholtz billows. *Geophys. Astrophys. Fluid Dynamics,* **10,** 53–87.

Scinocca, J. F., and W. R. Peltier, 1989: Pulsating downslope windstorms. *J. Atmos. Sci.,* **46,** 2885–2914.

Simard, A., and W. R. Peltier, 1982: Ship waves in the lee of isolated topography. *J. Atmos. Sci.,* **39,** 587–609.

Smith, R. B., 1985: On severe downslope winds. *J. Atmos. Sci.,* **42,** 2597–2603.

Sturrock, P. A., 1958: Kinematics of graving waves. *Phys. Rev.,* **112,** 1488.

Twiss, R. Q., 1951: On oscillations in electron streams. *Proc. Phys. Soc. London,* **64,** 654.